Micro-reinforced polymer composite materials studied by correlative X-ray imaging

Andrey Mikhaylov [a], Jorge Luis Beltran Diaz [a,*], Margarita Zakharova [a,b], Vitor Vinieska [a,c], Daniel Münch [a], Edwin Fohtung [d], Sergio Henrique Pezzin [e], Danays Kunka [a]

[a] Institute of Microstructure Technology (IMT), Karlsruhe Institute of Technology (KIT), Hermann-von-Helmholtz-Platz 1, Eggenstein-Leopoldshafen, 76344, Baden-Württemberg, Germany
[b] Center for Free-Electron Laser Science CFEL, Deutsches Elektronen-Synchrotron DESY, Notkestrasse 85, Hamburg, 22607, Germany
[c] Laboratory for Functional Polymers, Laboratory for Thin Films and Photvoltaics, Swiss Federal Laboratories for Materials Science and Technology (EMPA), Überlandstrasse 129, Dübendorf, 8600, Canton of Zürich, Switzerland
[d] Department of Materials Science and Engineering, Rensselaer Polytechnic Institute, 110 8th St, MRC 213, Troy, 12180, New York, United States of America
[e] Center of Technological Sciences, State University of Santa Catarina, R. Paulo Malschitzki, 200 - Zona Industrial Norte, Joinville, 89219-710, Santa Catarina, Brazil

ARTICLE INFO

ABSTRACT

Three-dimensional insights into the microstructure of composite materials are vital for enhancing their performance under operational conditions. Phase-sensitive methods can offer supplementary data, especially for materials with low absorption, compared to standard absorption-based techniques. This work presents the correlative X-ray imaging and computed tomography results of polymer composites reinforced with glass fibers using an inverted Hartmann mask. This method identified areas with enhanced refraction and scattering due to glass fibers and discriminated signals based on their orientation, offering an advantage in evaluating anisotropic materials. The simplicity of the setup, adding the inverted Hartmann mask, makes integration feasible in commercial CT scanners and existing radiography laboratories, enabling simultaneous phase, scattering, and absorption information extraction. Our approach, which combines refraction and scattering with absorption signals, exposes intricate structures beyond the usual spatial resolution threshold. Despite the distinct absorption coefficients of air, polymer-based, and glass fibers, the inverted Hartmann mask is crucial for examining similar absorption composites and low-absorbing materials. This research offers profound insights into the microstructures of fiber-reinforced polymer composites, laying the groundwork for studies of nanostructured functional composite materials.

1. Introduction

Studies on composite materials with tailored structures are of great interest in material science [1–6]. Polymer composites with glass fibers exhibit high strengths and low specific weights. The mechanical properties of glass-fiber-reinforced polymers are defined by the interaction between the fibers and matrix. Technological advances in techniques to improve material performance have led to new characterization approaches for studying fiber-reinforced polymer composites [7–9].

Imaging modalities that utilize the high penetration ability of X-rays, such as radiography, phase-sensitive X-ray imaging, and CT, are powerful tools for revealing the inner structure of such materials [10–19]. Previous studies have used μCT to study the internal microstructure of woven glass fiber composites, including tow architecture [20], microcracking [21], and three-dimensional visualizations [22]. Although X-ray absorption tomography is a valuable tool, in the case of low absorbing materials or materials with similar absorption coefficients, phase, and scattering imaging modalities could offer additional increased feature detectability [10,12,14,23,24] and information about fiber orientation [11,25–28].

Single-shot techniques have been adapted to tomographic settings because of their competitive advantage in terms of image acquisition time, such as single-shot speckle tracking [29–31] or adapting various optical elements such as arrays of zones [28,32,33] and Talbot Array Illuminators [34] including tomography at synchrotrons.

One of the ways to perform single-shot multi-contrast X-ray imaging

---

* Corresponding author.
  E-mail address: jorge.beltran@partner.kit.edu (J.L. Beltran Diaz).

at laboratory sources is to use a Hartmann/inverted Hartmann mask [35,36] or a Shack-Hartmann sensor for hard X-rays [37]. A single optical element acts as a wavefront modulator represented by arrays of apertures, pillars, or microlenses underlying the essence of the proposed method. There are two main approaches to retrieve contrasts using Hartmann or Shack-Hartmann sensors: FFT (Fast Fourier Transformation) routine [38] and two-dimensional Gauss peak fitting [37]. One reference image with an optical element and no object is required to retrieve three imaging modalities. Relaxed requirements for the spatial coherence of the beam, high visibility, low absorption, and simple implementation in both laboratory [35,36,39] and synchrotron [40–43] sources with only one optical element in the beam path make this method very promising. Within this method, one could benefit from either a large field of view and higher spatial resolution or higher flux efficiency by choosing between a Hartmann-like mask and the Shack-Hartmann approach.

We reported a study of flat composite samples reinforced with glass fibers in the same laboratory environment (cone beam configuration) [39]. To extend the imaging capabilities of the method and obtain three-dimensional information, we conducted tomography measurements of bulk composites. In this study, for the first time, we demonstrate the results of single-shot multi-contrast X-ray imaging and tomography of glass-fiber-reinforced polymer composites using an inverted Hartmann mask in a laboratory environment.

2. Materials and methods

2.1. Materials and composite fabrication

Epoxy resin RenLamë M, with diglycidyl ether bisphenol A (DGEBA) as main component, hardener (Aradur HY956-2), with triethyltetramine (TETA) as main component, were purchased from Huntsman (Sao Paulo, SP, Brazil). Plain weave type E-glass fiber fabric (ABCOL Brasil Compsitos Ltda) was used as reinforcement, with 300 g/m^2 and a density of 2.50 g/cm^3.

2.2. Composite description

Epoxy matrix composite specimens were prepared at GRUPOL-UDESC by vacuum-infusion molding. A stainless-steel mold (150 150 6 mm) was covered with a thin polyvinyl acetate layer. Afterward, ten layers of plain weave glass fiber fabric, approximately 40% of the total composite volume, were placed on the mold, which was closed with a 25

mm thick tempered glass plate. Polymer composite was composed of plain weave glass fiber (GF) and epoxy resin (60/40 m/m, fiber volume fraction = 39.33%). Composites were produced by mixing DGEBA epoxy resin (RenLamë M) with the curing agent (Aradur HY956-2) in a 5:1 (m: m) ratio, as recommended by the manufacturer. The specimens were produced with dimensions of (50 50 6 mm) for mechanical measurements and later cut to about (4.40 x 3.46 x 5.26 mm) for X-ray imaging.

2.3. Experimental setup

Multi-contrast X-ray imaging and tomography data sets were acquired at the Computed Lamiography/Computed Tomography Laboratory of the Institute for Photon Science and Synchrotron Radiation (IPS) at the Karlsruhe Institute of Technology (KIT). The imaging setup consisted of a microfocus X-ray tube (XWT-225, X-RAY WorX, Garbsen, Germany) with a tungsten target. An X-ray source was operated at the 60 kVp voltage and 3 W target power which, according to the manufacturer, results in a focal point size of approx. 1 μm. The detector was a unit Perkin Elmer XRD 1621 flat panel coupled to a Gadox scintillator, which has a 200 μm physical pixel size and a 40 x 40 cm area. Exposure time was 4 seconds per frame. For tomography measurements, 1024 projections over 180 degrees were acquired. Fig. 1 depicts the experimental setup.

We have used the same setup described in Mikhaylov et al. (2022) [39] with the addition of a rotary stage. Inverted Hartmann mask had 10 μm period, duty-cycle of 0.5, and an average height of 45.92 $\pm$ 0.07 μm, allowing to maximize spatial resolution. The visibility shows a high average value of 0.46. Distance from the source to the inverted Hartmann mask D1 was approx. 11 mm, source-to-sample distance D2 was 26 mm, and source-to-detector distance D3 was approx. 1500 mm. The mentioned setup allows us to achieve a mask magnification of approx. 140X (projected period of 1400 μm), with a sampling of 7 pixels per period of the mask.

We performed the optimization procedure as proposed in Bennett et al. (2010) [44] to achieve setup parameters allowing minimal penumbral blur (equation 1) and avoid phase wraparound artifacts (equation 2) with bounding condition (equation 3) to resolve the projected period of the mask:

$$\frac{s}{P} \cdot \frac{D_2}{D_3} << 1, \tag{1}$$

$$\frac{s}{P} \cdot \frac{(D_3 - D_2 - D_1)D_1}{D_2 D_3} > 1, \tag{2}$$
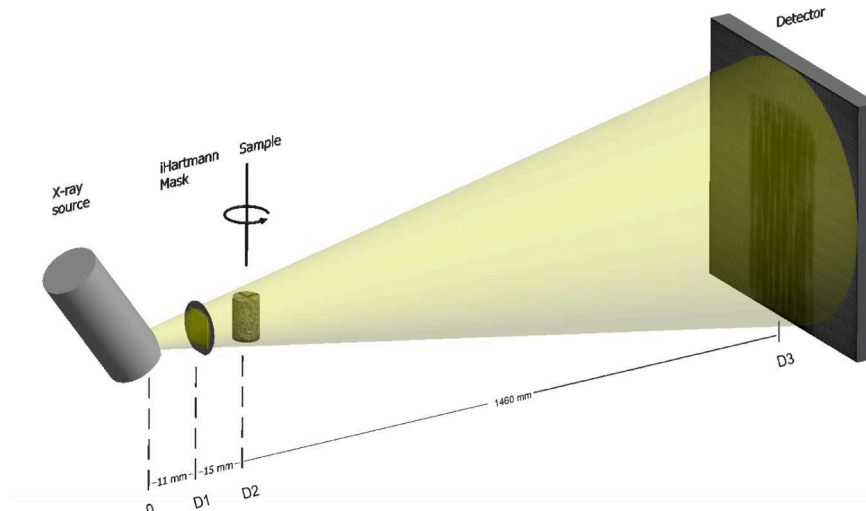

Fig. 1. Diagram illustrating the laboratory setup for single-shot multi-contrast X-ray imaging and tomography. Distances from the X-ray source are marked as: D1 for the inverted Hartmann mask, D2 for the sample, and D3 for the detector.

$$\frac{D_3 \cdot P}{3 \cdot s} > D_1. \tag{3}$$

where s is the focal spot size of the X-ray tube, P is the period of the iHM (Fig. 1). Solving the optimization problem, the penumbral blur at the detector plane for the mask was approx. 150 μm, for the imaging of the polymer composite was 75 μm. Taking into account the physical size of the detector unit, the effect of blurring on the spatial resolution for the mask and the object in the setup can be neglected.

Multi-contrast retrieval procedure was performed utilizing the FFT routine [38]. Wavefront reconstruction was achieved using the zonal method based on a modified Southwell algorithm with 10 iterations [45, 46]. Directional scattering in both directions combined using equation 4 under the condition of isotropic small-angle scattering:

$$Im_{scattering} = \frac{Im_{scatt,x} + Im_{scatt,y}}{2}, \tag{4}$$

where $Im_{scatt,x}$ and $Im_{scatt,y}$ are one-directional scattering images. Modification of FBP (Filtered Back Projection) algorithm for cone-beam geometry, known as FDK method [47], with ramp filtration was used for tomography reconstruction of absorption and scattering data.

The spatial resolution, defined by the period of the inverted Hartmann mask projected on the detector, is 24 μm. By using the equation 5, we estimate the phase detection limit to be 0.06 μrad.

$$\alpha_{min} = \frac{PS(D_1 + D_2)}{D_3(D_1 + D_2 + D_3)} \cdot I_{noise} \tag{5}$$

Therefore, the reconstructed volume consists of 246 $\times$246 $\times$246 voxels with a voxel size of 24 μm $\times$ 24 μm $\times$ 24 μm and a volume of 205.79 mm^3. The point of origin, with respect to which we will specify slicing, is a relative point that is located in Fig. 5(a), 7(a), and 8(a) in the lower-left corner for axes x and y, and in Fig. 5(b,c), 6(b,c) and 8(b,c) in the lower-left corner for axis z. Another way to imagine the point of origin is to think of it as the closest lower-left corner of the reconstructed volume, the frontal facet of which is attributed to angle 0.

3. Results

3.1. Multi-contrast single-shot X-ray imaging

Initially, images were recorded from the mask's periodic pattern as projected onto the detector to retrieve absorption information and details about phase and scattering through spatial harmonics analysis, which utilizes the Fourier Transform. Subsequently, reference samples composed of DGEBA epoxy resin (RenLamë M) with small glass fibers and curing agent Aradur HY956-2, were evaluated using multiple contrast X-ray imaging. These images, detailed in Fig. 2, include a) absorption contrasts, b) bidirectional scattering, and c) bidirectional phase. This figure is a referential basis for evaluating changes in absorption, refraction, and scattering signals when introducing glass fiber reinforcements.

Fig. 3 (a,b,c) shows projections in absorption contrast. Due to the tailored design of the glass-fiber-reinforced composites, we clearly see a difference in structure between *en face* and *en profile* projections. Fig. 3 (d,e,f) shows bidirectional scattering contrast, and (g,h,i) retrieved phase maps reveal areas with high scattering and refraction signals corresponding to the glass fiber bundles. The interfaces between plain weave fabric tows and resin-rich areas are clearly distinguishable at 173.52 degrees (Fig. 3(c,f)). The presence of the ten layers of glass fiber fabric can be noticed, where tows and deformations are identifiable. Although the spatial resolution of the setup is not enough to resolve single separate fibers, the presence of scattering and refraction indicates the inhomogeneity of the area. On the contrary, absorption projections do not reveal structural information and show just a difference in the density of the material (for the full range of absorption projections, see supplementary video S1). Fabric-reinforced composites can usually present internal microstructure defects, such as voids, fiber misalignment, and resin-rich regions, which can be caused by poor resin impregnation, residual thermal stress, and out-of-plane stitching [22]. It is worth to note the evident presence of phase retrieval artifacts in the background of the phase-contrast images in Fig. 3(g,h,I).

In areas near the bottom part of the sample in fig. 3(e), one might notice a decrease in the scattering signal. In the corresponding area in Fig. 3(h), representing phase image, a similar pattern arises. It might be explained by the transition between scattering and phase signals under certain conditions, such as the relative position of the fiber or fiber bundles [48,49]. Although the profile absorption projection Fig. 3(b) shows a uniformly composed material with good density homogeneity, scattering projection Fig. 3(e) and phase projection Fig. 3(h) reveals the inhomogeneous distribution of signals.

Fig. 4 shows differential phase (a,b,c) and scattering signal (d,e,f) in the vertical direction at the projection angles 162.25, 168.39, and 175.08 degrees. A background correction was performed to exclude the impact of intensity gradient using Fiji software[50]. Due to the design of the polymer composite sample and experimental setup, scattering and refraction signals are mixed. Projections reveal complementary information regarding glass fiber distribution. Refraction under angles below the angular resolution of the setup contributes to the scattering contrast available with this method [39,48]. In the case of glass fiber-reinforced polymer composite, refraction and scattering occur at the same locations. This effect happens due to the slightly different morphology, size, and alignment of the glass fibers in the bundle. The refraction signal appears at the edges of the fiber agglomerates. In addition, the glass fibers directly unsolvable by the measuring system show a prominent scattering signal due to their different orientations.

Special attention should be paid to the fact that fibers oriented under a slight angle to the optical axis of the setup generate strong refraction and scattering signals. In contrast, for the differential phase and scattering in the vertical direction, we do not record a prominent signal in areas where fibers are vertically oriented. It could be explained by the directional sensitivity of the imaging with an inverted Hartmann mask. This approach can be potentially explored for imaging anisotropic materials. It is possible to focus on one type of feature orientation by suppressing the signal from one of the directions by the alignment of the sample relative to the optical axis (see supplementary materials: differential phase and scattering in vertical direction videos S2 and S3,
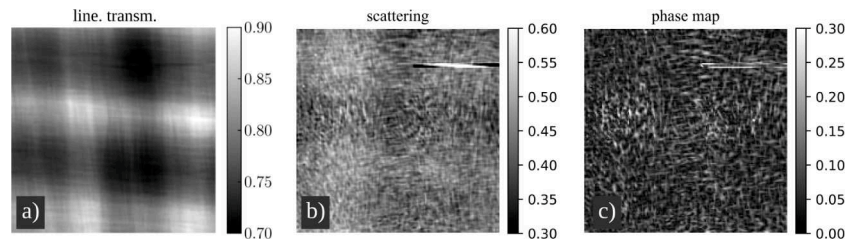

Fig. 2. Multi-contrast single-shot X-ray imaging of a polymer matrix with glass fibers, serving as a reference sample. a) Depicts contrasts in absorption (linearized transmission), while b) illustrates bi-directional scattering, and c) presents a bi-directional phase (phase map).
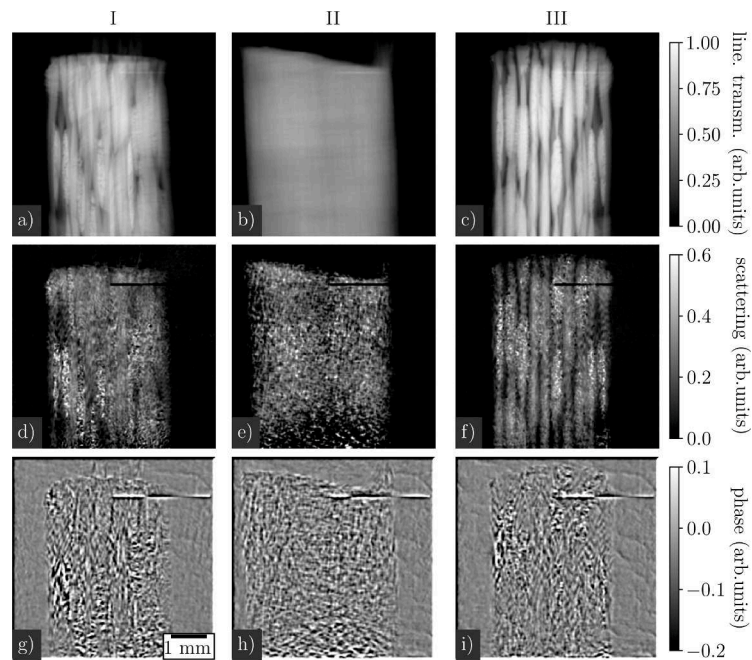
Fig. 3. Multi-contrast single-shot X-ray imaging of a polymer composite. The images present contrasts in absorption (linearized transmission) in panels (a,b,c), bidirectional scattering in panels (d,e,f), and integrated phase in panels (g,h,i). These images correspond to angles of 0, 90, and 173.52 degrees, labeled as I, II, and III, respectively. The bright white sections in images (a,b,c) highlight the glass fiber bundles due to their higher absorption properties. These areas, when observed in phase and scattering contrasts, exhibit increased refraction and scattering signals. Notably, a line of defective pixels can be discerned on the upper right corner of each image. Additionally, the background of phase images (g,h,i) displays retrieval artifacts. A scale bar is provided in the image (g) for reference.
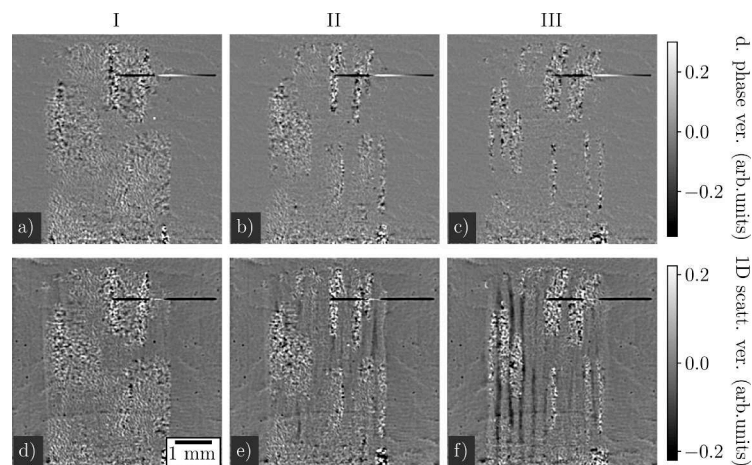

Fig. 4. Differential phase images (a,b,c) and scattering signal (d,e,f) oriented vertically, corresponding to angles 162.25, 168.39, and 175.08 degrees, labeled as I, II, and III, respectively. Notably, there are segmented signals indicative of glass fiber bundles, which are oriented within a narrow range relative to the X-ray propagation axis. The scale bar can be found in image (d).

respectively). The projection of the sample does not allow one to assess the quality of the polymer composite fabrication procedure. Possible imperfections such as air bubbles, cracks, and misrun defects are not visible on projection due to the composite's complex structure, the presence of the refractive and scattering media, and the low absorbing properties of the defects. We conducted tomography measurements to perform the all-around examination of the inner structure.

3.2. Absorption and scattering tomography of the polymer composite

Fig. 5 shows absorption and scattering tomography slices in positions 2.54, 2.52, and 3.72 mm relative to the point of origin of the composite sample for transverse, coronal, and sagittal planes, respectively. One could notice three different density media in the polymer composite: air-

containing regions, resin-rich areas with polymer matrix material (media boundaries marked with yellow arrows), and average absorption approx. 10 times higher than air and glass fiber material with an average absorption of approx. 17 times higher than air.

The presence of the molding and curing flaws is clear. air-containing defect with approx. 450 μm radius, marked with white arrows, was chosen as a reference point for the slicing. Other smaller air-containing defects vary in radius from 75 μm to 120 μm. Resin-rich areas and air do not show prominent scattering signals due to the absence of scattering centers in contrast to glass fiber bundles. Fig. 6 illustrates presence of air-containing defects and shows line profiles along marked lines. Regions marked with blue lines allows to visually link 2D image with 1D line profile.

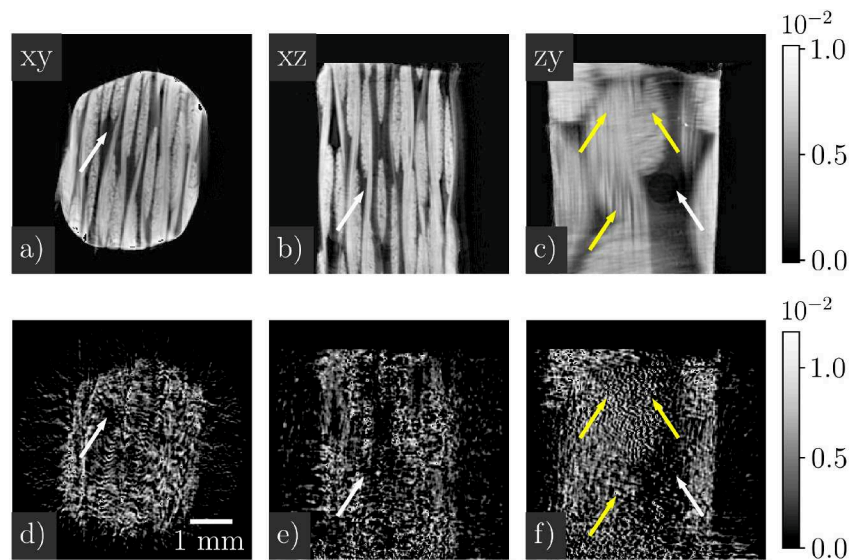Fig. 7 shows absorption and scattering tomography slices 3.17, 2.93,

Fig. 5. Tomographic slices showing absorption (a, b, c) and scattering (d, e, f). In the upper left, markers denote the slicing planes: xy for the transverse plane, xz for the coronal plane, and zy for the sagittal plane. The white arrows highlight an air-containing defect with an approximate radius of 450 μm, which was not discernible in the projections. Yellow arrows demarcate the boundaries between media of differing densities. A scale bar is provided in image (d).
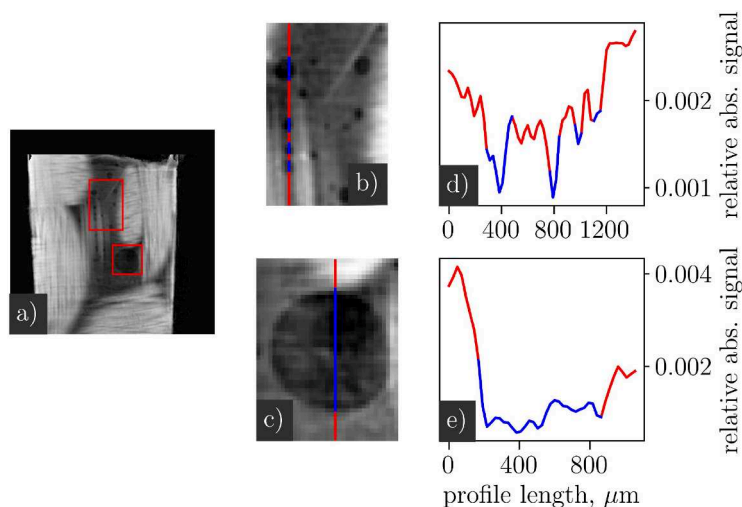

Fig. 6. Detailed features in a tomographic slice highlighting manufacturing imperfections. a) Provides an overall view of the slice tomography. b) Offers a zoomed view of the area marked by the upper rectangle. c) Shows a zoomed view of the area marked by the lower rectangle, with d) and e) presenting their respective line profiles to estimate the radius of local features indicative of manufacturing imperfections. Blue lines are utilized to visually link the profiles of bubbles/imperfections with the 2D image, facilitating size estimation using a calibrated scale.

and 2.66 mm relative to the point of origin of the composite sample for transverse, coronal, and sagittal planes, respectively. White arrows signalize the intersection of slicing planes. On the zy-slice, one could see the borders of the resin-rich areas. Scattering tomography slice Fig. 7(i) shows a significant scattering signal in the lower-left corner of the area signalized with a red arrow compared to the resin-rich area marked with a yellow arrow. This increase of scattering might be interpreted as the presence of a thin layer of the glass fibers that is barely visible on absorption tomography Fig. 7(c). Resin-rich areas and air-containing defects exhibit, on average, similar scattering signals. At the same time, the scattering signal retrieved in glass fiber-containing regions is approx. 8 times higher.

Fig. 8 shows absorption and scattering tomography slices 2.42, 3.19, and 3.22 mm relative to the point of origin of the composite sample for transverse, coronal, and sagittal planes, respectively. White arrows signalize the intersection of slicing planes. The zy-slice shows orthogonal bundles of glass fibers. They give a prominent absorption and

scattering signal. Scattering and density distribution are in good compliance. In the Fig. 8(f), a prominent scattering signal appears in the area marked with a yellow arrow. The same area in Fig. 8(c) has a slightly increased absorption signal. That could be explained by the presence of a thin layer of glass fibers, similar to the one signalized by the red arrow in Fig. 7(c,i).

Segmentation of the acquired tomographic data was performed using Fiji software [50] and open-source 3D Slicer software, version 4.11.2 [51,52].

Fig. 9 (a) shows a very characteristic profile of the plain weave fabric layers present in the composite, while Figs. 9(b,c,d), taken on transverse, coronal, and sagittal planes, respectively, evidence boundaries of volume of interest inside the composite structure. As shown by the render of the volume of interest (Fig. 9a), segmentation of the absorption signal associated with voluminous glass fiber agglomerates works well in the mentioned composite. This is due to the high difference between absorption signals of glass fibers bundles, polymer base, and air, as stated
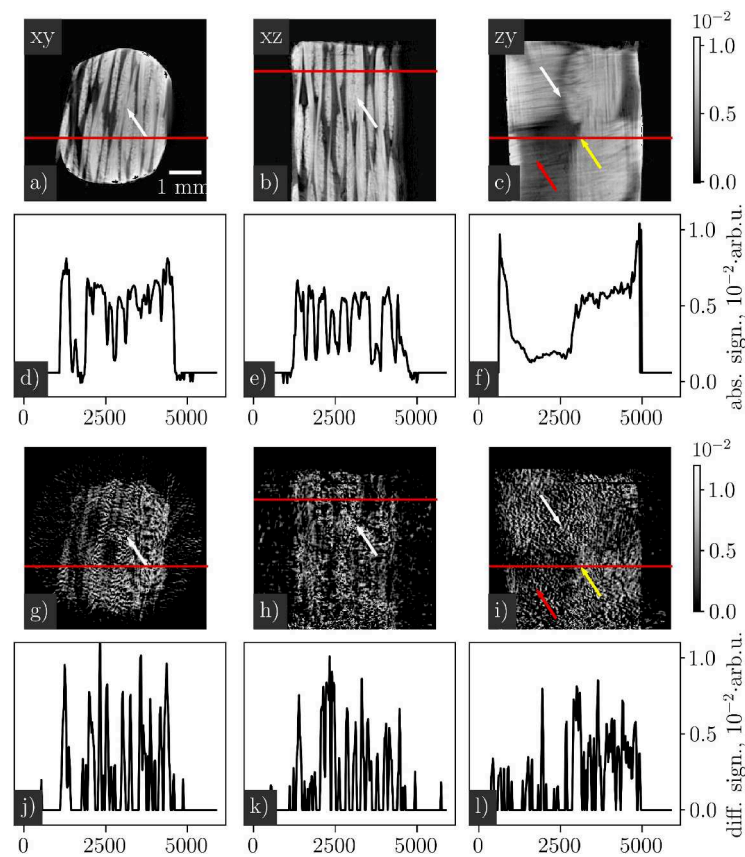
Fig. 7. Tomographic slices (a,b,c,g,h,i) and line profiles (d,e,f,j,k,l) for absorption and scattering, demonstrating the strength of scattering signals in the presence of fiber bundles. Slices a), b), and c) with their respective line profiles d), e), and f) for absorption. Slices g), h), and i) with their respective line profiles j), k), and l) for scattering. The white arrows highlight where the slicing planes intersect. The red arrow points to a thin layer of scattering media, while the yellow arrows denote the boundary of a distinct resin-rich area. A scale bar can be found in the image (a).
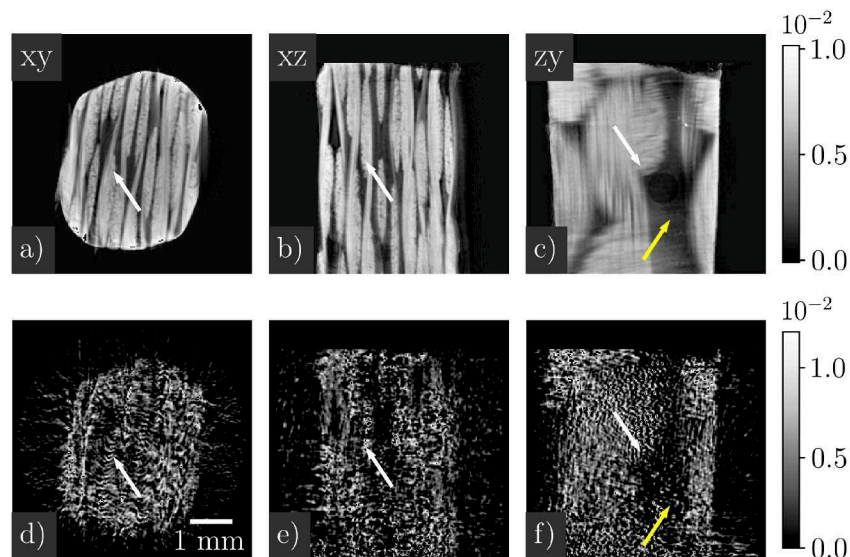

Fig. 8. Tomographic slices showcasing absorption (a, b, c) and scattering (d, e, f). The annotations in the upper left define the slicing directions: xy for the transverse plane, xz for the coronal plane, and zy for the sagittal plane. White arrows highlight the intersections of the slicing planes. A discernible air-containing defect, approximately 495 μm in radius and previously unseen in projections, is evident. The yellow arrow points to a thin layer of glass fibers that contribute to the scattering signal. A scale bar is included in image (d).

in section 3.2. However, the segmentation of separate thin layers that exhibit poor absorption signals could be a challenging task. The information on fiber orientation could be extracted from the bidirectional scattering and differential phase signals (Fig. 4) and volumetric scattering data (figures 5,8(d,e,f) and Fig. 7(g,h,i)). Applying approaches similar to those described by Kim et al. ([28]), this method can serve as a
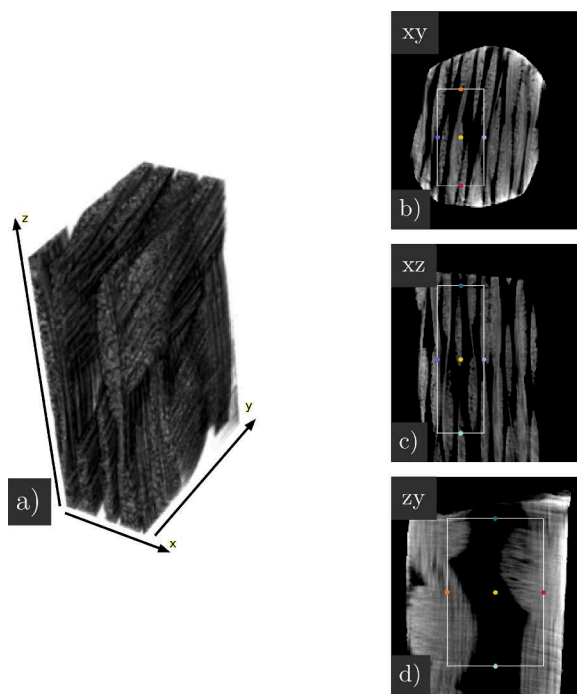
Fig. 9. Segmentation of the glass fiber bundles derived from absorption tomography data. Image (a) presents the volume of interest, while (b), (c), and (d) display the transverse, coronal, and sagittal planes, respectively, highlighting the specified region of interest.

multipurpose tool for predicting the behavior of composite materials with tailored structure and the volumetric data can be used in computer modeling ([16–18]). In addition, this method opens a new window to distinguish among composites with similar absorption cross-sections and low-absorbing materials.

4. Conclusion

This study pioneered the utilization of multi-contrast X-ray imaging and computed tomography using an inverted Hartmann mask to explore fiber-reinforced polymer composite materials in laboratory settings. While only absorption signals facilitate the segmentation of areas with varied absorption properties, they do not delve deeply into structural intricacies. Incorporating refraction and scattering data reveals detailed structures, including those beneath the spatial resolution. Notably, even when the material in question exhibits distinct absorption coefficients for air, polymer base, and glass fibers, the inverted Hartmann mask's inclusion proves valuable, especially when examining composites with analogous absorption or those with minimal absorption properties. This not only facilitates structural segmentation and discrimination at the physical level but also underscores the method's unique capabilities.

Through tomography, we identified density variances, such as air-filled defects and resin-rich zones that possess absorption rates approximately 10 times greater than that of air. Moreover, glass fiber bundles demonstrated absorption approximately 17 times more than air and produced scattering signals almost 8 times stronger than those from air or resin-rich areas. This heightened scattering signal accentuates the visibility of thin bundle layers with minimal absorption. Notably, air-containing defects, with radii spanning from 75 μm to 495 μm, were obscured in projections due to the dominating media possessing potent absorption, refraction, and scattering attributes. A significant advantage of our proposed method lies in its simplicity, necessitating just a single shot and a singular optical element. As such, it's adaptable to various X-ray infrastructures, ranging from large-scale entities like synchrotrons to basic laboratory setups and even readily available commercial systems.

Introducing these imaging modalities could revolutionize micro- and nanostructured material research by offering deeper insights into their structural intricacies, functional traits, and potential applications.

CRediT authorship contribution statement

Andrey Mikhaylov: Conceptualization, Data curation, Formal analysis, Methodology, Software, Supervision, Validation, Visualization, Writing – original draft, Writing – review & editing. **Jorge Luis Beltran Diaz:** Conceptualization, Data curation, Formal analysis, Funding acquisition, Investigation, Methodology, Project administration, Resources, Software, Supervision, Validation, Visualization, Writing – original draft, Writing – review & editing. **Margarita Zakharova:** Conceptualization, Investigation, Methodology, Software, Writing – review & editing. **Vitor Vinieska:** Conceptualization, Investigation, Methodology, Software, Writing – review & editing. **Daniel Münch:** Resources. **Edwin Fohtung:** Visualization, Writing – review & editing. **Sergio Henrique Pezzin:** Conceptualization, Resources, Writing – review & editing. **Danays Kunka:** Project administration, Investigation, Visualization, Supervision, Validation, Investigation, Methodology, Writing – review & editing.

Declaration of competing interest

The authors declare that they have no known competing financial interests or personal relationships that could have appeared to influence the work reported in this paper.

Supplementary material

Supplementary material associated with this article can be found, in the online version, at 10.1016/j.nwnano.2024.100035

References

[1] N. Saba, M. Paridah, M. Jawaid, Mechanical properties of kenaf fibre reinforced polymer composite: a review, Construct. Build. Mater. 76 (2015) 87–96.

[2] S.S. Pendhari, T. Kant, Y.M. Desai, Application of polymer composites in civil construction: a general review, Compos. Struct. 84 (2) (2008) 114–124.

[3] M. Ma, L. Guo, D.G. Anderson, R. Langer, Bio-inspired polymer composite actuator and generator driven by water gradients, Science 339 (6116) (2013) 186–189.

[4] G. X Gu, I. Su, S. Sharma, J.L. Voros, Z. Qin, M.J. Buehler, Three-dimensional-printing of bio-inspired composites, J. Biomech. Eng. 138 (2) (2016).

[5] S. Ramakrishna, J. Mayer, E. Wintermantel, K.W. Leong, Biomedical applications of polymer-composite materials: a review, Compos. Sci. Technol. 61 (9) (2001) 1189–1224.

[6] C.Y.X. Chua, H.-C. Liu, N. Di Trani, A. Susnjar, J. Ho, G. Scorrano, J. Rhudy, A. Sizovs, G. Lolli, N. Hernandez, et al., Carbon fiber reinforced polymers for implantable medical devices, Biomaterials 271 (2021) 120719.

[7] W. Stark, M. Jaunich, J. McHugh, Dynamic mechanical analysis (dma) of epoxy carbon-fibre prepregs partially cured in a discontinued autoclave analogue process, Polym. Test. 41 (2015) 140–148.

[8] J. Feng, Z. Guo, Temperature-frequency-dependent mechanical properties model of epoxy resin and its composites, Composites Part B: Eng. 85 (2016) 161–169.

[9] R. Murugan, R. Ramesh, K. Padmanabhan, Investigation on static and dynamic mechanical properties of epoxy based woven fabric glass/carbon hybrid composite laminates, Procedia Eng. 97 (2014) 459–468.

[10] T. Davis, D. Gao, T. Gureyev, A. Stevenson, S. Wilkins, Phase-contrast imaging of weakly absorbing materials using hard x-rays, Nature 373 (6515) (1995) 595–598.

[11] F. Prade, F. Schaff, S. Senck, P. Meyer, J. Mohr, J. Kastner, F. Pfeiffer, Nondestructive characterization of fiber orientation in short fiber reinforced polymer composites with x-ray vector radiography, NDT & E Int. 86 (2017) 65–72.

[12] S. Senck, M. Scheerer, V. Revol, K. Dobes, B. Plank, J. Kastner, Non-destructive evaluation of defects in polymer matrix composites for aerospace applications using x-ray talbot-lau interferometry and micro ct. 58th AIAA/ASCE/AHS/ASC Structures, Structural Dynamics, and Materials Conference, 2017, p. 0355.

[13] N. Morimoto, H. Kimura, T. Shirai, T. Doki, S. Sano, A. Horiba, K. Kitamura, Talbot–lau interferometry-based x-ray imaging system with retractable and rotatable gratings for nondestructive testing, Rev. Sci. Instrument. 91 (2) (2020) 023706.

[14] J. Glinz, J. Šleichrt, D. Kytýř, S. Ayalur-Karunakaran, S. Zabler, J. Kastner, S. Senck, Phase-contrast and dark-field imaging for the inspection of resin-rich areas and fiber orientation in non-crimp vacuum infusion carbon-fiber-reinforced polymers, J. Mater. Sci. 56 (16) (2021) 9712–9727.

[15] S. Garcea, Y. Wang, P. Withers, X-ray computed tomography of polymer composites, Compos. Sci. Technol. 156 (2018) 305–319.

[16] G. Nikishkov, Y. Nikishkov, A. Makeev, Finite element mesh generation for composites with ply waviness based on x-ray computed tomography, Adv. Eng. Softw. 58 (2013) 35–44.

[17] M.W. Czabaj, M.L. Riccio, W.W. Whitacre, Numerical reconstruction of graphite/ epoxy composite microstructure based on sub-micron resolution x-ray computed tomography, Compos. Sci. Technol. 105 (2014) 174–182.

[18] R. Sencu, Z. Yang, Y. Wang, P. Withers, C. Rau, A. Parson, C. Soutis, Generation of micro-scale finite element models from synchrotron x-ray ct images for multidirectional carbon fibre reinforced composites, Composites Part A: Appl. Sci. Manuf. 91 (2016) 85–95.

[19] M.J. Emerson, K.M. Jespersen, A.B. Dahl, K. Conradsen, L.P. Mikkelsen, Individual fibre segmentation from 3d x-ray computed tomography for characterising the fibre orientation in unidirectional composite materials, Composites Part A: Appl. Sci. Manuf. 97 (2017) 83–92.

[20] F. Desplentere, S.V. Lomov, D. Woerdeman, I. Verpoest, M. Wevers, A. Bogdanovich, Micro-ct characterization of variability in 3d textile architecture, Compos. Sci. Technol. 65 (2005) 1920–1930.

[21] P.J. Schilling, B.R. Karedla, A.K. Tatiparthi, M.A. Verges, P.D. Herrington, X-ray computed microtomography of internal damage in fiber reinforced polymer matrix composites, Compos. Sci. Technol. 65 (14) (2005) 2071–2078.

[22] A. Rashidi, T. Olfatbakhsh, B. Crawford, A.S. Milani, A review of current challenges and case study toward optimizing micro-computed x-ray tomography of carbon fabric composites, Materials 13 (16) (2020) 3606.

[23] T.-H. Le, P.J. Dumont, L. Orgéas, D. Favier, L. Salvo, E. Boller, X-ray phase contrast microtomography for the analysis of the fibrous microstructure of smc composites, Composites Part A: Appl. Sci. Manuf. 39 (1) (2008) 91–103.

[24] B. Yu, R. Bradley, C. Soutis, P. Withers, A comparison of different approaches for imaging cracks in composites by x-ray microtomography, Philos. Trans. R. Soc. A: Math. Phys. Eng. Sci. 374 (2071) (2016) 20160037.

[25] M. Bech, O. Bunk, T. Donath, R. Feidenhans, C. David, F. Pfeiffer, Quantitative x-ray dark-field computed tomography, Phys. Medicine Biol. 55 (18) (2010) 5529.

[26] T.H. Jensen, M. Bech, O. Bunk, T. Donath, C. David, R. Feidenhans, F. Pfeiffer, Directional x-ray dark-field imaging, Phys. Med. Biol. 55 (12) (2010) 3317.

[27] A. Malecki, E. Eggl, F. Schaff, G. Potdevin, T. Baum, E.G. Garcia, J.S. Bauer, F. Pfeiffer, Correlation of x-ray dark-field radiography to mechanical sample properties, Microscopy Microanal. 20 (5) (2014) 1528–1533.

[28] J. Kim, M. Kagias, F. Marone, M. Stampanoni, X-ray scattering tensor tomography with circular gratings, Appl. Phys. Lett. 116 (13) (2020) 134102.

[29] I. Zanette, T. Zhou, A. Burvall, U. Lundström, D.H. Larsson, M. Zdora, P. Thibault, F. Pfeiffer, H.M. Hertz, Speckle-based x-ray phase-contrast and dark-field imaging with a laboratory source, Phys. Rev. Lett. 112 (25) (2014) 253903.

[30] T. Zhou, H. Wang, K. Sawhney, Single-shot x-ray dark-field imaging with omnidirectional sensitivity using random-pattern wavefront modulator, Appl. Phys. Lett. 113 (9) (2018) 091102.

[31] K.M. Pavlov, H.T. Li, D.M. Paganin, S. Berujon, H. Rougé-Labriet, E. Brun, Single-shot x-ray speckle-based imaging of a single-material object, Phys. Rev. Appl. 13 (5) (2020) 054023.

[32] J. Kim, A. Slyamov, E. Lauridsen, M. Birkbak, T. Ramos, F. Marone, J. W. Andreasen, M. Stampanoni, M. Kagias, Macroscopic mapping of microscale fibers in freeform injection molded fiber-reinforced composites using x-ray scattering tensor tomography, Composites Part B: Eng. 233 (2022) 109634.

[33] M. Kagias, Z. Wang, P. Villanueva-Perez, K. Jefimovs, M. Stampanoni, 2d-omnidirectional hard-x-ray scattering sensitivity in a single shot, Phys. Rev. Lett. 116 (9) (2016) 093902.

[34] A. Gustschin, M. Riedel, K. Taphorn, C. Petrich, W. Gottwald, W. Noichl, M. Busse, S.E. Francis, F. Beckmann, J.U. Hammel, et al., High-resolution and sensitivity bi-directional x-ray phase contrast imaging using 2d talbot array illuminators, Optica 8 (12) (2021) 1588–1595.

[35] M. Zakharova, V. Vlnieska, H. Fornasier, M. Börner, T.d.S. Rolo, J. Mohr, D. Kunka, Development and characterization of two-dimensional gratings for single-shot x-ray phase-contrast imaging, Appl. Sci. 8 (3) (2018) 468.

[36] M. Zakharova, S. Reich, A. Mikhaylov, V. Vlnieska, M. Zuber, S. Engelhardt, T. Baumbach, D. Kunka, A comparison of customized hartmann and newly introduced inverted hartmann masks for single-shot phase-contrast x-ray imaging. EUV and X-ray Optics: Synergy between Laboratory and Space VI volume 11032, International Society for Optics and Photonics, 2019, p. 110320U.

[37] T. dos Santos Rolo, S. Reich, D. Karpov, S. Gasilov, D. Kunka, E. Fohtung, T. Baumbach, A. Plech, A shack-hartmann sensor for single-shot multi-contrast imaging with hard x-rays, Appl. Sci. 8 (5) (2018) 737.

[38] H.H. Wen, E.E. Bennett, R. Kopace, A.F. Stein, V. Pai, Single-shot x-ray differential phase-contrast and diffraction imaging using two-dimensional transmission gratings, Opt. Lett. 35 (12) (2010) 1932–1934.

[39] A. Mikhaylov, M. Zakharova, V. Vlnieska, A. Khanda, S. Bremer, M. Zuber, S. H. Pezzin, D. Kunka, Inverted hartmann mask made by deep x-ray lithography for single-shot multi-contrast x-ray imaging with laboratory setup, Opt. Express 30 (6) (2022) 8494–8509.

[40] S. Reich, T. dos Santos Rolo, A. Letzel, T. Baumbach, A. Plech, Scalable, large area compound array refractive lens for hard x-rays, Appl. Phys. Lett. 112 (15) (2018) 151903.

[41] M. Zakharova, S. Reich, A. Mikhaylov, V. Vlnieska, T. dos Santos Rolo, A. Plech, D. Kunka, Inverted hartmann mask for single-shot phase-contrast x-ray imaging of dynamic processes, Opt. Lett. 44 (9) (2019) 2306–2309.

[42] A.A. Mikhaylov, A. Plech, M. Zakharova, V. Vlnieska, D. Kunka, 2d lens array for multi-contrast x-ray imaging. EUV and X-ray Optics: Synergy between Laboratory and Space VI volume 11032, International Society for Optics and Photonics, 2019, p. 1103208.

[43] A. Mikhaylov, S. Reich, M. Zakharova, V. Vlnieska, R. Laptev, A. Plech, D. Kunka, Shack–hartmann wavefront sensors based on 2d refractive lens arrays and super-resolution multi-contrast x-ray imaging, J. Synchrotron Radiat. 27 (3) (2020) 788–795.

[44] E.E. Bennett, R. Kopace, A.F. Stein, H. Wen, A grating-based single-shot x-ray phase contrast and diffraction method for in vivo imaging, Med. Phys. 37 (11) (2010) 6047–6054, https://doi.org/10.1118/1.3501311.

[45] B. Pathak, B.R. Boruah, Improved wavefront reconstruction algorithm for shack–hartmann type wavefront sensors, J. Opt. 16 (5) (2014) 055403.

[46] S. Reich. Hierarchical Imaging of the Dynamics During Pulsed Laser Ablation in Liquids, KIT-Bibliothek, 2019. Ph.D. thesis.

[47] L.A. Feldkamp, L.C. Davis, J.W. Kress, Practical cone-beam algorithm, Josa a 1 (6) (1984) 612–619.

[48] L. Koenig, M. Zuber, B. Trimborn, T. Farago, P. Meyer, D. Kunka, F. Albrecht, S. Kreuer, M. Volk, M. Fiederle, et al., On the origin and nature of the grating interferometric dark-field contrast obtained with low-brilliance x-ray sources, Phys. Med. Biol. 61 (9) (2016) 3427.

[49] M. Esposito, L. Massimi, I. Buchanan, J. D. Ferrara, M. Endrizzi, A. Olivo, The transition from refraction to ultra-small-angle x-ray scattering (usaxs) in a laboratory phase-based x-ray microscope for soft tissue imaging. 15th International Conference on X-ray Microscopy (XRM2022), 2022.

[50] J. Schindelin, I. Arganda-Carreras, E. Frise, V. Kaynig, M. Longair, T. Pietzsch, S. Preibisch, C. Rueden, S. Saalfeld, B. Schmid, et al., Fiji: an open-source platform for biological-image analysis, Nature Method. 9 (7) (2012) 676–682.

[51] 3d slicer software, version 4.11, (http://www.slicer.org/). Accessed: 2023-06-22.

[52] A. Fedorov, R. Beichel, J. Kalpathy-Cramer, J. Finet, J.-C. Fillion-Robin, S. Pujol, C. Bauer, D. Jennings, F. Fennessy, M. Sonka, et al., 3d slicer as an image computing platform for the quantitative imaging network, Magnetic Resonance Imag. 30 (9) (2012) 1323–1341.